



## Quantitative live-cell imaging of lipidated peptide transport through an epithelial cell layer

Hundahl, Adam Colin; Weller, Arjen; Larsen, Jannik Bruun; Hjørringgaard, Claudia U.; Hansen, Morten B.; Müндler, Ann Kathrin; Knuhtsen, Astrid; Kristensen, Kasper; Arnsfang, Eva C.; Andresen, Thomas Lars

Total number of authors:  
12

Published in:  
Journal of controlled release

Link to article, DOI:  
[10.1016/j.jconrel.2023.01.066](https://doi.org/10.1016/j.jconrel.2023.01.066)

Publication date:  
2023

Document Version  
Publisher's PDF, also known as Version of record

[Link back to DTU Orbit](#)

### Citation (APA):

Hundahl, A. C., Weller, A., Larsen, J. B., Hjørringgaard, C. U., Hansen, M. B., Müндler, A. K., Knuhtsen, A., Kristensen, K., Arnsfang, E. C., Andresen, T. L., Mortensen, K. I., & Marie, R. (2023). Quantitative live-cell imaging of lipidated peptide transport through an epithelial cell layer. *Journal of controlled release*, 355, 122-134. <https://doi.org/10.1016/j.jconrel.2023.01.066>

---

### General rights

Copyright and moral rights for the publications made accessible in the public portal are retained by the authors and/or other copyright owners and it is a condition of accessing publications that users recognise and abide by the legal requirements associated with these rights.

- Users may download and print one copy of any publication from the public portal for the purpose of private study or research.
- You may not further distribute the material or use it for any profit-making activity or commercial gain
- You may freely distribute the URL identifying the publication in the public portal

If you believe that this document breaches copyright please contact us providing details, and we will remove access to the work immediately and investigate your claim.



# Quantitative live-cell imaging of lipidated peptide transport through an epithelial cell layer

Adam Coln Hundahl, Arjen Weller, Jannik Bruun Larsen, Claudia U. Hjørringgaard, Morten B. Hansen, Ann-Kathrin Mündler, Astrid Knuhtsen, Kasper Kristensen, Eva C. Arnspang<sup>1</sup>, Thomas Lars Andresen, Kim I. Mortensen, Rodolphe Marie\*

Technical University of Denmark, Department of Health Technology, Ørsted's Plads, Building 345C, DK-2800 Kgs. Lyngby, Denmark

## ARTICLE INFO

### Keywords:

Drug delivery  
Lipidated peptides  
Intestinal barrier transport  
Salmon calcitonin  
Caco-2 cells  
Quantitative imaging  
Transport mechanism

## ABSTRACT

Oral drug delivery increases patient compliance and is thus the preferred administration route for most drugs. However, for biologics the intestinal barrier greatly limits the absorption and reduces their bioavailability. One strategy employed to improve on this is chemical modification of the biologic through the addition of lipid side chains. While it has been established that lipidation of peptides can increase transport, a mechanistic understanding of this effect remains largely unexplored. To pursue this mechanistic understanding, end-point detection of biopharmaceuticals transported through a monolayer of fully polarized epithelial cells is typically used. However, these methods are time-consuming and tedious. Furthermore, most established methods cannot be combined easily with high-resolution live-cell fluorescence imaging that could provide a mechanistic insight into cellular uptake and transport. Here we address this challenge by developing an axial PSF deconvolution scheme to quantify the transport of peptides through a monolayer of Caco-2 cells using single-cell analysis with live-cell confocal fluorescence microscopy. We then measure the known cross-barrier transport of several compounds in our model and compare the results with results obtained in an established microfluidic model finding similar transport phenotypes. This verifies that already after two days the Caco-2 cells in our model form a tight monolayer and constitute a functional barrier model. We then apply this assay to investigate the effects of side chain lipidation of the model peptide drug salmon calcitonin (sCT) modified with 4-carbon and 8-carbon-long fatty acid chains. Furthermore, we compare that with experiments performed at lower temperature and using inhibitors for some endocytotic pathways to pinpoint how lipidation length modifies the main avenues for the transport. We thus show that increasing the length of the lipid chain increases the transport of the drug significantly but also makes endocytosis the primary transport mechanism in a short-term cell culture model.

## 1. Introduction

Therapeutic drugs administered by injection into the bloodstream have a high bioavailability [1] [2]. However, the need for injections lowers patient compliance [3]. Alternative administration routes such as nasal inhalation and, in particular, oral delivery increase the patient compliance and are thus increasingly explored [4] [5]. However, orally administered biopharmaceuticals must first reach the small intestine, pass through the mucus layer and cross the epithelial cell layer forming the intestinal barrier to finally reach the vascular system. Consequently,

the oral bioavailability of larger drugs, like peptides, is still suboptimal (around 1–2%) greatly limiting their therapeutic potential [6]. Strategies to improve bioavailability include packaging of the biopharmaceutical in nanoparticles to target the uptake via Clathrin-mediated endocytosis [7], use of permeation enhancers to co-transport the drug [8,9], or alteration of the chemical structure of the drug and promote a transport route of interest. Recently, the lipidation of peptides [10,11] has been shown to improve peptide bioavailability by promoting interactions of the drug with the cell membrane. For example, increasing the lipid chain length has been shown to improve on the overall

*Abbreviations:* sCT, salmon Calcitonin; PSF, Point Spread Function; TAT, Trans-activator of Transcription; PBS, Phosphate-buffered saline; ELISA, Enzyme-linked immunosorbent assay; EDTA, Ethylenediaminetetra-acetic acid.

\* Corresponding author.

E-mail address: [rcwm@dtu.dk](mailto:rcwm@dtu.dk) (R. Marie).

<sup>1</sup> University of Southern Denmark, Department of Green Technology, Campusvej 55, 5230 Odense M, Denmark.

<https://doi.org/10.1016/j.jconrel.2023.01.066>

Received 29 September 2022; Received in revised form 10 January 2023; Accepted 26 January 2023

Available online 3 February 2023

0168-3659/© 2023 The Authors. Published by Elsevier B.V. This is an open access article under the CC BY license (<http://creativecommons.org/licenses/by/4.0/>).

transport of salmon Calcitonin (sCT) [12], a calcium-regulating drug used to treat osteoporosis typically administered through injections. However, the mode of action is still largely unknown and needs to be investigated using in vitro cellular transport models.

The human epithelial colorectal adenocarcinoma cell line Caco-2 is used as a model of the gut epithelial cells for in vitro transport studies [13]. Caco-2 cells are cultured on a porous membrane filter separating an apical chamber on top of the membrane and a basolateral chamber on the bottom (Transwell plate). Cells are typically grown for 18–21 days with media change every 2–3 days before the cells organize into a polarized monolayer with tight barriers [14]. The overall transport is then typically quantified by an end-point measurement using mass spectrometry [15]. Several other methods based on surface capture of the analyte and subsequent optical detection including ELISA [16] are also used. While this approach has the advantage to be applicable to any drug without labelling, long cell culture time makes the experiment tedious and thus limits the applicability of the Transwell system for massively parallel studies and consequently leads to a trial-and-error approach to developing new drugs. Instead, fluorescence microscopy can be used to quantify the biopharmaceutical in the different compartments of the cell [17]. Fluorescence labeling of the biopharmaceutical combined with confocal imaging allows for quantifying the amount of drug transported through a monolayer of Caco-2 cells by end-point measurement of the concentration of the biopharmaceutical on the basal side. Additionally, the amount of fluorescence in the cytosol of the cells can be quantified by integrating intensity in a single  $z$ -plane thereby providing additional information [18]. Moreover, high magnification confocal fluorescence microscopy can help pinpoint the uptake mechanism of the biopharmaceutical. In some cases, a biopharmaceutical may appear as puncta, which can suggest that the uptake mechanism is mediated by endocytosis [19,20]. Using multicolor imaging and colocalization analysis, confocal fluorescence microscopy provides high spatial resolution, so it can reveal the biopharmaceuticals' interactions with organelles [21,22]. This was successfully used to investigate the transport of the peptide drugs such as insulin nanoclusters or gliadins [23,24]. Eventually, live-cell imaging can provide sufficient time resolution to also elucidate the kinetics of cellular uptake [25]. Still, the quantification of the transported peptide signal in a monolayer of cells may be complicated by the limited spatial resolution of fluorescence microscopy. Lateral resolution is approximately 200 nm, whereas axial resolution is much larger, around 400 nm at a 500 nm excitation, and it is so even for confocal imaging [26]. In a typical imaging experiment the objective is placed above or below the cell layer and so the overall transport through a cell layer is observed axially. In this geometry, quantifying the fluorescence signal from the cytosol or around the cell membrane cannot be done simply by, for example, integrating the intensity in a single  $z$ -plane. Indeed, the cell surrounding's fluorescence signal significantly extends within the cell's interior and vice versa. This challenge exists whether it appears as a diffuse signal indicating a release of the peptide in the cytosol, or as puncta-like signal typical of the peptide found primarily in endosomes, for example resulting from endocytosis [19]. Eventually, the signal from fluorescent molecules located outside the cell on both sides of the cell layer, i.e., the apical and basolateral sides, would overlap when the thickness of the cell approaches that of the size of the Point Spread Function (PSF), making image interpretation difficult. In this context, deconvoluting fluorescence images with the PSF [26] is a way to extract the fluorescence intensity in the different compartments of the cell. It has been used to quantify the fluorescence of puncta-like structures, typically in experiments where transport occurs via endosomes [27]. Still, little has been done to quantify the diffuse signal from the cell cytosol and any localized signal from the membrane [28]. Particularly, there is a potential to use PSF deconvolution in combination with a physical model of the cell to extract all contributions to the overall fluorescence signal simultaneously.

Here we quantify the signal of the lipidated forms of the 3.4 kDa

peptide salmon calcitonin in a layer of Caco-2 cells by first measuring the PSF of the spinning disc microscope and then using this knowledge to perform an axial deconvolution of fluorescence intensity profiles measured through the Caco-2 cells. The deconvolution is combined with a simple physical model of the cell to interpret the fluorescence intensity of the cytosol, the cell membrane, and the transported molecule across the cell monolayer. We confirm the validity of the cellular model for comparative studies by measuring the known transport properties of the Trans-activator of Transcription (TAT) peptide, using dextran, and Lucifer Yellow as negative controls, i.e. molecules for which there is no active transport. We show how the axial intensity profile through a cell looks like in different uptake scenarios. We then quantified the transport of the native sCT and two double-lipidated sCT analogs over 4 h using spinning disc confocal fluorescence microscopy to quantify the effects of lipidation on the transport of sCT. Furthermore, we show differences in the transport pattern of the peptide by adding an inhibitor for endocytosis and lowering the temperature below physiological temperatures. We show that despite the limitation of short-term cell cultures in terms of biological complexity and in vivo translatability, this model is applicable for comparative studies where systematic variations of peptide properties are studied. Overall, using in vitro live-cell fluorescence imaging and a comprehensive data analysis, we show that the transport of sCT is altered qualitatively and quantitatively by double lipidations and that increasing chain length from 4 to 8 carbons makes endocytosis the primary transport mechanism.

## 2. Results

### 2.1. Cellular model and axial PSF deconvolution scheme

We aim to employ fluorescence live-cell imaging to quantify the transport of a fluorescently labelled peptide through a cell monolayer mimicking the intestinal barrier. To this end, we use time-lapse spinning disc confocal microscopy to image Caco-2 cells exposed to the labelled peptide of interest. Caco-2 cells are first seeded in a commercial 8-well plate suitable for oil immersion imaging (Ibidi) and incubated for 48 h. The cell's nucleus and the plasma membrane are then stained using Hoechst (blue) and CellMask (red), respectively (Fig. 1A). Next, the drug of interest, labelled with a fluorophore, is added right before time-lapse imaging starts. Three-colour confocal  $z$ -stacks are acquired every 40 min for 4 h at multiple  $x$ - $y$  positions (Fig. 1B). Within each field-of-view (FOV), we select a few cells and define one 10-by-10  $\mu\text{m}$  region of interest (ROI) per cell. Two axial intensity profiles are extracted for each cell in this ROI: one for the membrane, and one for the peptide (Fig. 1C-D). Each intensity profile is deconvoluted separately with the point spread function (PSF) of our spinning disc microscope.

While models exist for the lateral and axial PSF, we ensure that the PSF is accounting for any aberrations of our set-up by using a measurement of the PSF estimated for each fluorescence channel using 100-nm polymer beads (Fig. S1).

We then look at the intensity profile in the red channel i.e. for the membrane stain. The cell membranes are much thinner than the PSF and thus appear as two Gaussian-like intensity peaks, which coincide with the position of the bottom and top membrane of the cell (Fig. 1C). In this model we assume that the membranes are horizontal within the ROI. We thus make sure to choose the ROI in each cell away from the nucleus.

Our data show that each cell's cytoplasm is thin ( $<5 \mu\text{m}$ ) compared to the axial resolution of the spinning disc microscope (Fig. 2), hence the two PSF peaks are not readily resolved. In such a situation, the peptide signal from the bottom of the cell, the cytosol and the solution overlap in an axial intensity profile. This highlights the need to perform an axial PSF deconvolution of the peptide signal to quantify the amount of peptide in the cytoplasm and any fluorescence located between the cells and the surface that supports them.

We use the fitted positions of the cell's membrane to divide the intensity profile of the peptide channel into four sections that are relevant

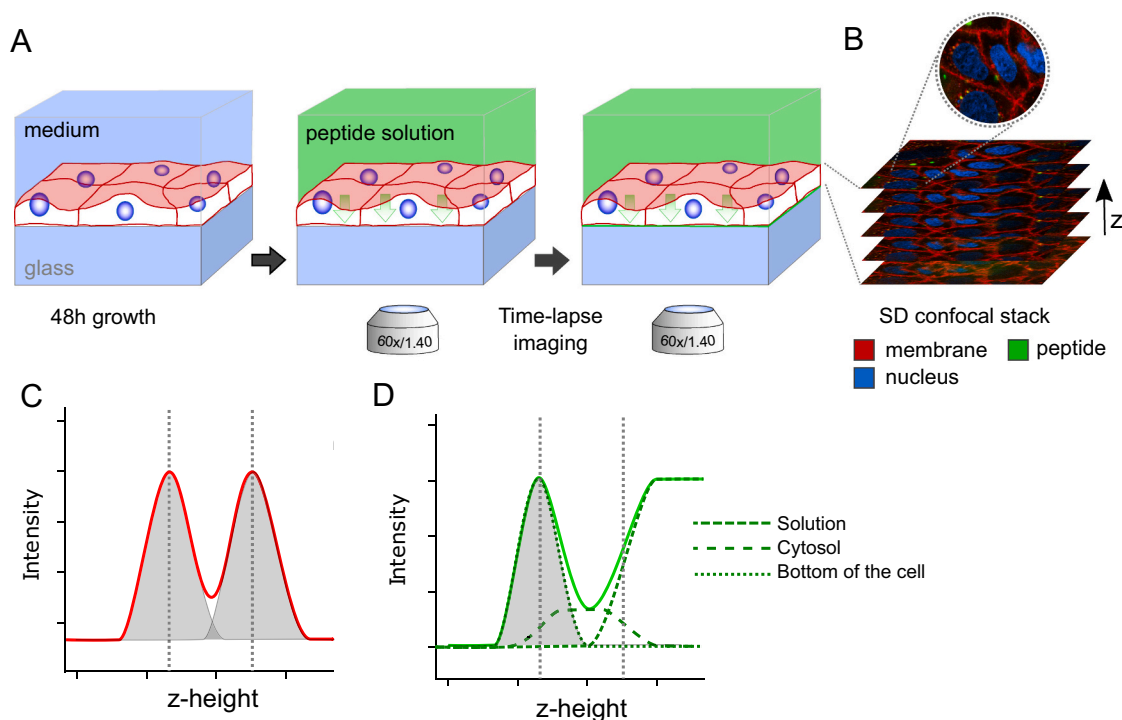


**Fig. 1.** Assay for peptide transport imaging with spinning disc confocal microscopy of live cells A) Caco-2 cells are grown on a glass surface then exposed to fluorescently labelled peptide. B) Timelapse confocal imaging yields confocal stacks in three colors. Axial intensity profiles of C) the membrane channel and D) the peptide channel shown as continuous lines. They are deconvoluted with the experimental PSF (grey) to extract the position of the cell membranes (vertical dotted lines) and the peptide signal (dotted and dashed line) in the solution, the cytosol, and the bottom of the cell representing the accumulated peptide at the bottom cell membrane. (For interpretation of the references to colour in this figure legend, the reader is referred to the web version of this article.)

for quantifying how much peptide is transported through the cell monolayer: 1) the solution above the cell 2) the cytosol, 3) the bottom membrane of the cell, and 4) the glass. Here we note two things about the space between the cell and the glass: one, it must contain cellular junk accumulated during the 2 days growth. Second, it is much narrower than the resolution of the microscope, and so we cannot discriminate between peptide bound to the cell's bottom membrane and any fluorescence trapped between the cell and the glass surface. Hence, in the following, we will refer to this fluorescence signal as ‘colocalizing’ with the bottom membrane of the cell.

With that in mind, we model the peptide intensity in each section and derive the corresponding analytical expression describing the intensity signal (see Methods). Essentially, our physical model accounts for the following four effects: First, the signal from the peptide solution extends significantly into the cell and even the glass substrate (Fig. 1D). We assume a uniform concentration in the solution and model this contribution as a step function at the top membrane convolved with the axial PSF. Second, we assume the peptide concentration is uniform in the cytosol (Fig. 1D). As a result, this contribution is modeled as a step function at the bottom membrane and another step function at the top membrane convolved with the PSF. Third, as argued previously, the space above the glass and below the bottom membrane is shallow compared to the PSF and cannot be resolved by confocal scanning so that any peptide present here yields a PSF-like peak that colocalizes with the bottom membrane. Last, the fluorescence signal of the solution and the cells extends significantly into the glass due to the overlap of the illumination through the many pinholes of the Nipkow disc [26]. It varies slowly in space, so, for simplicity, we consider it constant and subtract this background from the rest of the intensity profile. Summing the intensity contributions from these four sections results in an expression we can use to fit the axial intensity profile in the peptide channel (Fig. 1D).

## 2.2. Time-lapse imaging and axial intensity profile reveal transport of Fluorescein-labelled TAT (TAT-FITC)

To validate our assay, we first performed a positive control with a peptide that we know is capable of cross-barrier transport. We use Fluorescein-labelled Trans-Activator of Transcription (TAT-FITC), previously shown to cross the intestinal barrier [29]. We added 3.5  $\mu\text{M}$  of TAT-FITC to the Caco-2 cells and recorded z-stacks every 40 min for 240 min.

Fig. 2A shows the xz-projection of a single cell in a FOV for selected time points: 1) before adding peptide, 2) at  $t = 0$  being immediately after adding the peptide and readjusting z-focus and x-y position to correct for addition-mediated drift, 3)  $t = 120$  min, and 4)  $t = 240$  min. Prior to addition of the peptide, we detect two red peaks in the membrane signal (red) close together, representing the two membranes of the cell, a low background fluorescence in the peptide channel (green) fluctuating around the background level (Fig. 2B). Note that we also show the intensity of the blue channel across the nucleus i.e. outside the ROI. Here also note that the red channel reveals the presence of puncta-like structures in the cytoplasm that are more densely packed around the nucleus. In our analysis we sample intensity profiles away from the nucleus to access the content of the cytoplasm minimizing the influence of the organelles around the nucleus. We see that the addition of the peptide in solution leads to an overall increase in the peptide intensity level in all four sections (in solution, in the cytosol, at the interface at the bottom of the cell and in the glass) on the xz-cross section image at  $t = 0$  min. This general increase is also seen in the intensity profiles sampled in the ROI (Fig. 2B), underscoring the importance for devising our model capable of decoupling the contributions from the individual sections. Strikingly, we detect a strong peptide signal colocalizing with the interface at the bottom of the cell suggesting that TAT has passed the cell membrane and reached the bottom of the cell layer (Fig. 2A-B). The signal at the bottom of the cell is already present immediately after TAT-

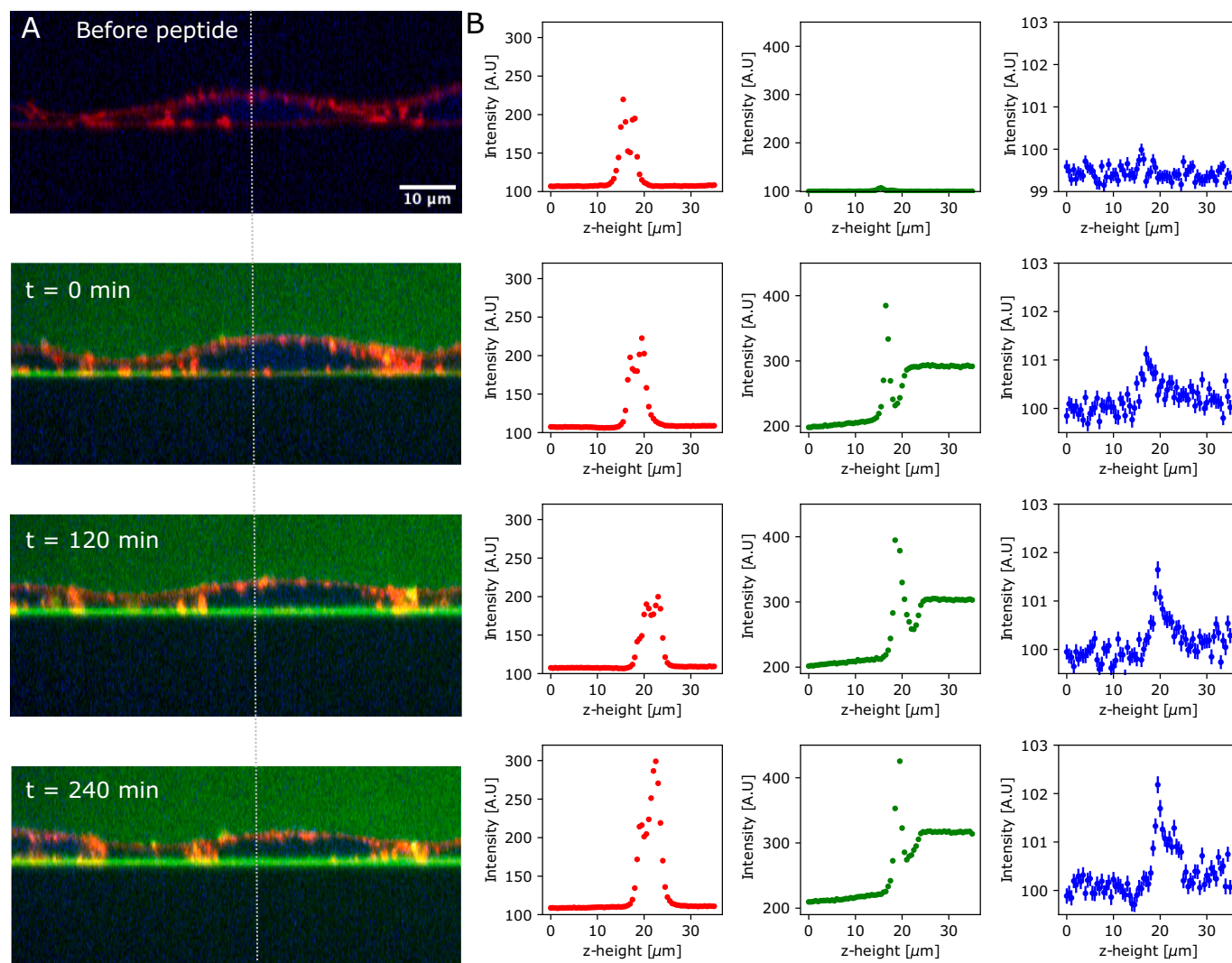


**Fig. 2.** Live-cell imaging shows the accumulation of TAT-FITC signal under the Caco-2 cell layer. A)  $xz$  projection of the same cell at four different time points, i.e. before addition of the labelled peptide and at  $t = 0$ , 120, and 240 min. B) Intensity profiles for the membrane (red), peptide (green) and nucleus (blue) fluorescent channels. The intense green spike developing over time indicates accumulation of the peptide at the bottom of the cell layer. (For interpretation of the references to colour in this figure legend

FITC is added to the solution and it seems as if the amplitude of the peak of intensity at the bottom of the cell remains constant for the rest of the experiment (240 min). However, we will now show using PSF deconvolution that it in fact increases with time after an initial abrupt increase, thus illustrating how our assay facilitates live-cell imaging that can provide the intensity input necessary for creating an analytical model that can quantitatively describe peptide transport across a cellular barrier.

### 2.3. Fluorescence model allows quantification of the cellular transport of TAT

We first fit the plasma membrane signal axial intensity profile through one ROI at  $t = 0$  (Fig. 3A) using our model for the membrane signal (red) being two PSF-shaped peaks. From this fit we extract the position of the top and bottom membrane (dashed vertical lines in Fig. 3A). We then use the membrane positions to fit the peptide signal (green) with our model (Fig. 3B) and extract the intensity of the peptide signal in solution, in the cytosol and below the cell (Fig. 3C). Here, the peptide signal colocalized with the bottom membrane appears as a single PSF-shaped peak. This initial signal below the cells appears instantaneously (less than a few minutes) and is observed for all

molecules we tested (TAT, sCT, Dextran, Lucifer yellow) in similar order of magnitude (4 to 10 intensity units) and so it cannot have the same origin as the later time dependent change we observe in terms of dynamics and magnitude. Due to its suddenness, we rule out a cellular transport mechanism to be involved and focus our attention on the subsequent change of this signal over the course of the experiment (240 min). To this end we measured a new  $z$ -stack every 40 min allowing us to quantify the cross-barrier peptide transport over time. Comparing the intensity profiles for the same cell after 240 min of incubation (Fig. 3D-F) with the ones found right after TAT is added (Fig. 3A-C) we see that the peak-like signal corresponding to the TAT-FITC signal under the cells indeed has increased, although it is neither readily seen from the images (Fig. 2A) nor from the raw intensity profiles (Fig. 2B). Next, we performed a deconvolution at all time points allowing us to simultaneously follow the peptide intensity change in solution, in the cytosol and at the interface at the bottom of the cell (Fig. 3G). Performing the analysis for 10 different ROIs/cells in parallel we found a constant peptide intensity in the solution over time, as we would expect (blue, Fig. 3G), but a linear increase in the cytosol reaching a 25-fold increase when comparing the value at  $t = 0$  versus  $t = 240$  min (red, Fig. 3G). Finally, we found that the TAT-FITC signal colocalized with the bottom membrane increased two-fold from the first measurement until  $t = 100$  min, before reaching a

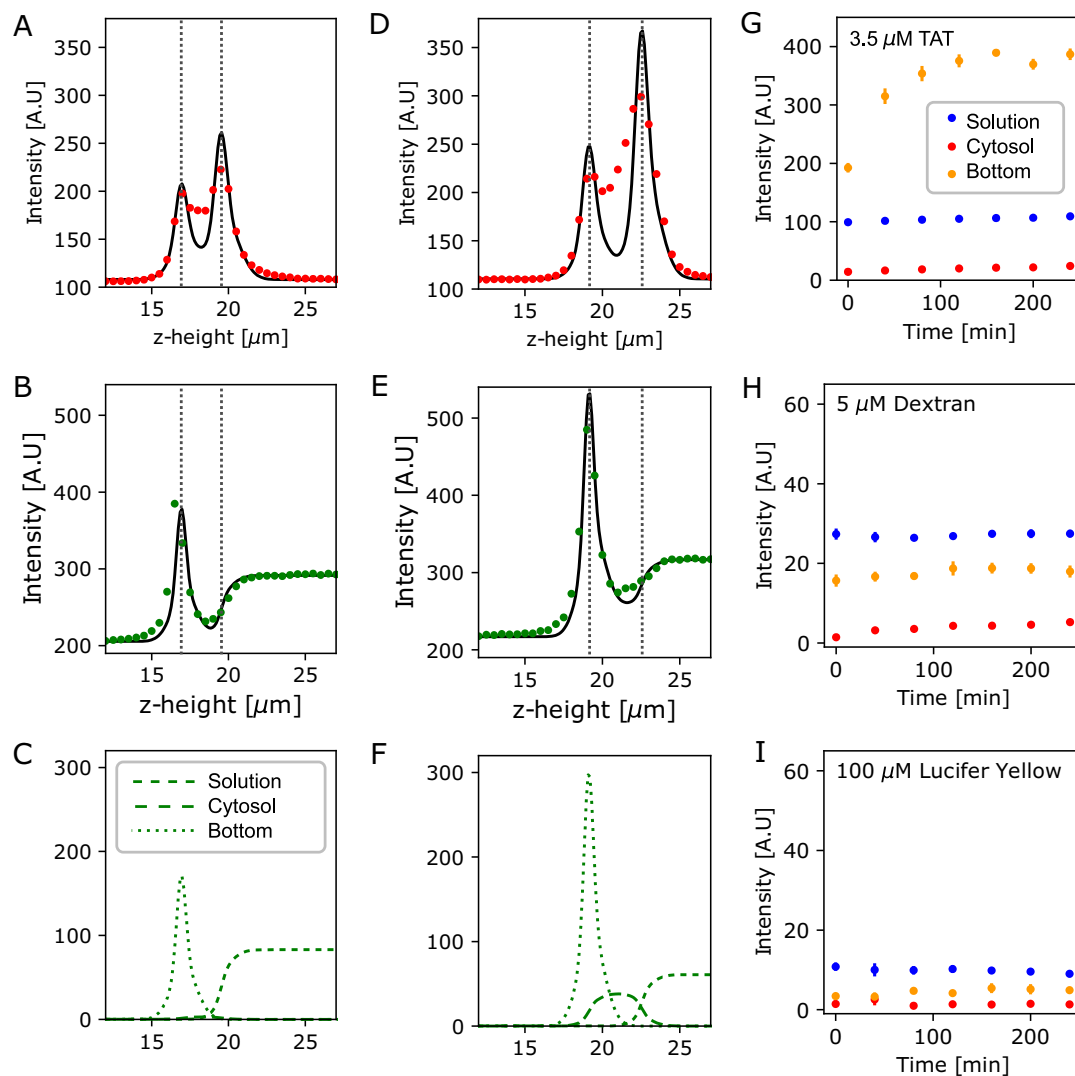


**Fig. 3.** Validation of the cellular model and the axial PSF deconvolution scheme. A) Membrane intensity (dots) and fit (full line) yielding the position of the cell membrane (dotted line) at  $t = 0$ . B) Peptide signal intensity (dots) and fit (line) under the incubation with 3.5  $\mu\text{M}$  TAT-FITC at  $t = 0$ . C) Individual components of the fit to the peptide signal showing the peptide signal in the solution, the cytosol and at the bottom of the cell. D–F) Same graphs as in A–C) but at  $t = 240$  min. G) The TAT-FITC intensity at the bottom of the cell (orange), in solution (blue) and in the cytosol (red) as a function of time,  $N = 10$  cells. H) Same as G but for the experiment with Dextran-FITC,  $N = 12$  cells. I) Same as G but for the experiment with Lucifer Yellow,  $N = 5$  cells. Error bars are standard error of the mean (s.e.m.). (For interpretation of the references to colour in this figure legend, the reader is referred to the web version of this article.)

plateau (orange, Fig. 3G). Using our assay, we can measure a time dependent transport of TAT that corroborates earlier findings that it is able to transport to the bottom cell membrane of Caco-2 cells [19].

It has been proposed that the main transport mechanism of TAT is via endocytosis at the 3.5  $\mu\text{M}$  concentration that we use in our experiment [19]. Hence, we expect the signal at the bottom of the cell to result from vesicular transport and accumulation near the bottom membrane. From our data, we can only pinpoint that the TAT-FITC signal is colocalized with the bottom membrane but cannot conclude whether the TAT-FITC is free in solution, bound to the membrane, or shed out of the cells in extracellular vesicles. However, we do observe that the TAT-FITC signal measured in the cytosol increases 25 times in the course of 240 min. This signal is measured away from the puncta-like features around the cell's nucleus. This shows that TAT is in fact taken up by the cell.

To ensure that the detected transport of TAT-FITC to the bottom of the cell layer is not just an artifact of a non-tight barrier, we employed two classical reporter molecules of barrier integrity [30]. Keeping the same experimental setup as used for the TAT-FITC experiment, we first added 5  $\mu\text{M}$  of 4.4 kDa dextran-FITC and quantified the intensity signal in solution, in the cytosol and at the bottom of the cell over time

(Fig. 3H). We chose this specific dextran molecular weight to match the molecular weight of TAT. As seen for TAT, the solution intensity is constant over time. The cytosolic dextran content increases slightly from 2 to 4 A.U. over 4 h, which has also been seen for a Transwell experiment with a similar duration [31]. Interestingly, we detect no significant increase of the dextran-FITC signal colocalizing with the bottom membrane of the cell, which shows that dextran does not accumulate at the bottom of the cells over time. To ensure a comprehensive validation of the barrier integrity of our model, we also performed a time course experiment where 100  $\mu\text{M}$  Lucifer Yellow (400 Da) is added to the cells (Fig. 3I). Lucifer Yellow is much smaller than TAT or Dextran. We found that the fluorescence signal at the bottom of the cell layer is unchanged throughout the experiment, confirming that the cell layer is leak-tight even for smaller molecules than TAT. From those two control experiments, we conclude that the increase of the TAT-FITC signal being colocalized with the bottom membrane of the cells (Fig. 3G orange dots) is a result of an accumulation of TAT-FITC at the bottom of the cell layer mediated by a directional transport.

#### 2.4. Double lipidation of sCT increases peptide amounts colocalizing with the bottom membrane

Next, we implemented the imaging assay to perform a detailed investigation of how cross-barrier transport of the pharmaceutically relevant peptide salmon calcitonin (sCT) was modified by double lipidations of varying length. Labelling with a fluorophore is necessary to our imaging assay but can influence the properties of the peptide and its transport [15,32]. We thus choose to label the sCT using the fluorophore Atto488, a choice guided by the low membrane interaction factor of this fluorophore [33]. We tested three analogs of sCT labelled with Atto488 at the N-terminus: sCT(C0/C0) that is modified only with Atto488, sCT(C4/C4) that is modified with two C4 chains, and sCT(C8/C8) that is modified with two C8 chains (Fig. S2). Solution FCS and stepwise single-molecule bleaching experiments both confirm that all sCT analogs are almost exclusively found as monomers in the condition used for imaging (see Supplementary Information).

The axial intensity profiles obtained for the three sCT analogs are qualitatively similar to the profiles obtained with TAT. Fig. S3A and D show representative examples of intensity profiles through single ROIs before the addition of sCT(C0/C0) and after 240 min incubation. After fitting of the intensity profiles for several ROIs, we follow the evolution of the intensity in the solution, the cytosol and at the bottom of the cell layer with time for the three analogs (Fig. S3). We look closer at the intensity of the peptide colocalizing with the bottom membrane (Fig. 4) as this was found to increase significantly for cells incubated with TAT-FITC (Fig. 3). We see a linear increase of the sCT(C0/C0) signal over 4 h corresponding to approximately a 1.5-fold change of the initial signal. Similarly, the addition of sCT(C4/C4) yield a 1.5-fold change (Fig. 4). For both analogs, the level of accumulated peptide at the bottom of the cells does not exceed the solution level. Furthermore, the peptide signal detected in the cytosol is constant indicating that the cytosolic content does not increase over time although the peptide reaches the bottom of

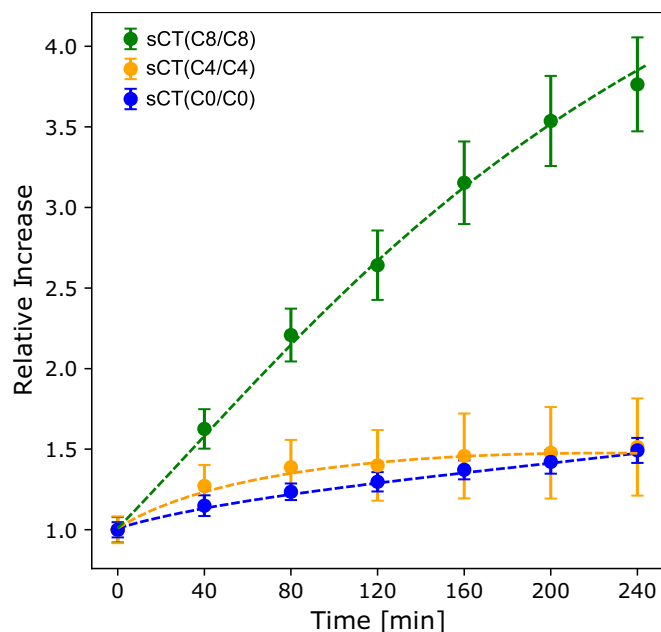


**Fig. 4.** The relative increase of the peptide signal colocalized with the bottom membrane of the cell shown for the three sCT analogs over time. The relative difference in peptide signal at the interface at the bottom of the cell calculated by normalizing all time points with the intensity immediately after peptide addition at  $t = 0$  for sCT(C0/C0) (blue,  $N = 24$ ), sCT(C4/C4) (orange,  $N = 38$ ) and sCT(C8/C8) (green,  $N = 38$ ). Dashed lines are for guidance of the eye. Error bars are standard error of the mean (s.e.m.). (For interpretation of the references to colour in this figure legend, the reader is referred to the web version of this article.)

the cell. This suggests that the peptide is transported towards the bottom of the cells by a mechanism not involving release to the cytosol. In contrast, the sCT(C8/C8) signal at the bottom of the cell increases steadily over 4 h and reaches a value much higher than the level detected in the solution corresponding to a 3.7 times relative increase. As for the other two sCT analogs, we detect no significant change of the cytosol signal, hence we interpret this as the sCT(C8/C8) not being released inside the cytosol either (Fig. S3, panel I). The results summarized in Fig. 4 show that our assay based on cells grown on glass for 2 days and an axial PSF deconvolution scheme can be used to quantify differences in transport of lipidated peptides.

The Caco-2 cells are grown for 2 days, which is short compared to the state-of-the-art, where Caco-2 cell differentiation and polarization is typically 21 days. Although faster polarization, down to 3 days, has been reported [16,34], it is important to note that short term cell cultures of Caco-2 cannot recapitulate all biological functions of the gut epithelial. Here we use a cellular model in a comparative study focusing on ensuring critical functions such as barrier integrity, and to validate the models applicability we applied our image analysis scheme on  $z$ -stacks acquired on fully differentiated cells. To this end, we used a commercial organ-on-a-chip platform [35] to grow Caco-2 cells for 4 days under alternate flow conditions. The organ-on-a-chip platform is compatible with high NA microscopy so we can readily apply our imaging assay to the Caco-2 cells grown in the device. We have recently shown that due to the flow conditions, differentiation is increased and that this leads to polarized cells with tight junctions. We have also shown that the Caco-2 cells tube inside the microfluidics channel recapitulates the transport properties of TAT-FITC [36]. We then expose the cells to the labelled peptides and proceed to imaging as for our assay. The intensity profiles acquired through single ROIs are similar to the profiles obtained in our simple cellular model on glass (Fig. S4). We note that an initial sudden increase of signal below the cell is also detected in this case, with similar amplitudes so we can rule out pure diffusion through a leaky barrier as the origin of this signal. We repeat the experiment for all three sCT analogs and proceed to axial PSF deconvolution to extract the time variation of the peptide signal in the solution, the cytosol, and the bottom of the cells (Fig. S5). In the case of fully polarized cells, the relative increase of the signal for sCT(C8/C8) is somewhat lower (2.2 times) than for the cells grown on glass (3.5 times), however, lipidation of the sCT also increases transport, leading to an increased peptide signal colocalizing with the bottom of the Caco-2 cell monolayer. This is an important validation that our assay based on short-time grown cells is sufficient for a quantitative comparison of the overall transport properties of the lipidated peptides in a minimal gut-model. To verify that the differences in transport to the bottom membrane are significantly different between the three analogs we did a Kruskal-Wallis test followed by a post hoc pairwise Mann Whitney [37]. With an acceptance level of 0.05, sCT(C8/C8) is significantly different ( $p < 0.05$ ) from sCT(C4/C4) and sCT(C0/C0), but sCT(C4/C4) and sCT(C0/C0) are not significantly different from each other ( $p = 0.65$ ) (Fig. S6 A).

#### 2.5. Temperature and endocytosis inhibitors affect the transport mechanisms of sCT analogs

Next, we use our assay to address how lipidation affects the transport mechanism of sCT. We repeated our experiment for the three sCT analogs either in the presence of Dynasore or at a decreased temperature (25 °C). Both perturbations are well-described ways to reduce the endocytic uptake into cells [38–41]. We added 80  $\mu$ M Dynasore, an inhibitor of the Clathrin- and Caveolin-mediated endocytosis pathway, which is active in Caco-2 cells [42]. Dynasore has previously been shown to inhibit the endocytotic transport of small nanoparticles by approximately 50 to 60% at this concentration [43]. In particular, Dynasore is acting within minutes [39] of the addition to the cells and is thus particularly suited to use in our imaging assay. We then compare the relative increase of the signal at the bottom of the cells after 240 min

incubation with labelled peptides at 37 °C, and at 25 °C and 37 °C in the presence of Dynasore (Fig. 5 and Fig. S7). Our main observation is that the addition of Dynasore is mostly reducing the transport of the sCT(C8/C8) ( $3.7\times$  to  $2.5\times$ ), and to a lesser extent reducing the transport of the unlipidated sCT ( $1.5\times$  to  $1.2\times$ ). The relative transport of sCT(C4/C4) was not affected by Dynasore. This is in contrast with the effect of temperature that reduces the transport of all three analogs.

A Kruskal-Wallis test and a post hoc test reveal that there is a significant difference in the transport with or without Dynasore for sCT (C8/C8) and sCT(C0/C0), however not for sCT(C4/C4) (Fig. S6 B–D). As for the experiment at lowered temperature, transport was significantly lowered for all three analogs.

We conclude first that all peptides are affected when energy-dependent uptake is diminished using temperature, suggesting that this is important for transport. Here we note that both active cellular transport and passive transport through the membrane are being affected by the reduced temperature. Secondly, the transport of sCT(C8/C8) depends on the Clathrin and Caveolin pathways to a larger extent than does the transport of sCT with shorter lipid chains sCT(C4/C4). This illustrates how even small changes in lipid length can greatly affect which pathway is mediating transport.

While Fig. 4 showed that the transport of sCT can be increased by a factor of 2.5 by lipidating sCT with two C8 chains, Fig. 5 suggests that our cellular model combined with live-cell imaging and image analysis is able to show differences in the transport mechanism by using inhibitors of cellular transport pathways. That said, the axial resolution of confocal imaging is still preventing us to pinpoint if the signal of the bottom of the cell originates from peptide inside the cell, below the cell, free in solution on either side of the cell bottom membrane or associated with it. Thus, to address this, we incubated the cells with sCT(C8/C8) for 4 h, washed the excess peptide with PBS and then shrunk the cells by disrupting the tight junctions using  $1.5\ \mu\text{M}$  EDTA (Fig. 6A). This allowed

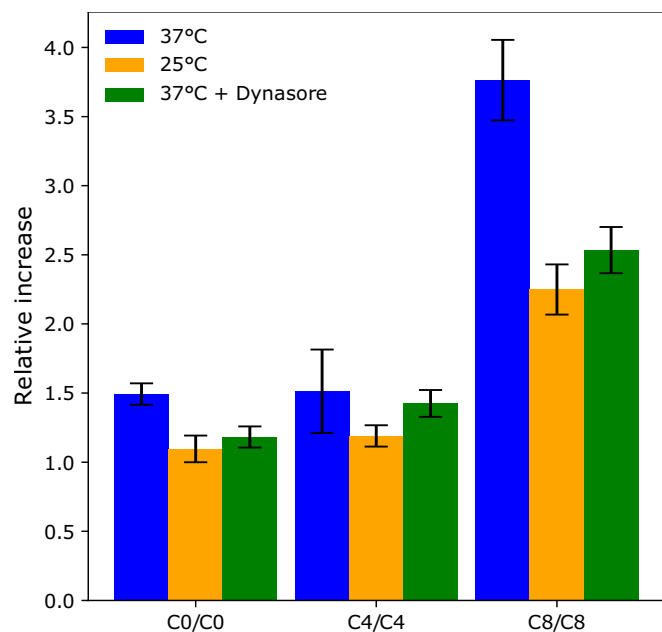


**Fig. 5.** Temperature and endocytosis inhibitor Dynasore change the relative transport of sCT analogs. Relative increase of the peptide signal at the bottom of the cells measured at  $t = 240$  min for sCT(C0/C0), sCT(C4/C4) and sCT(C8/C8). The blue bars represent the relative increase at 37 °C ( $N = 24, 38$  and  $38$ ). The orange bars represent the relative increase at the reduced temperature of 25 °C ( $N = 24, 20$  and  $19$ ). The green bars represent the relative increase at 37 °C with  $80\ \mu\text{M}$  Dynasore added. Here  $N = 18, 17$  and  $31$  for sCT(C0/C0), sCT(C4/C4) and sCT(C8/C8), respectively. (For interpretation of the references to colour in this figure legend, the reader is referred to the web version of this article.)

us to measure intensity profiles for cells just after the addition of EDTA and then after 10 min incubation (Fig. 6B and C). Here we see that at the same position on the glass, the intensity profile shows the same intensity peak colocalizing with the bottom of the cell when the cell is here as when the cell has shrunk, and the plasma membrane has partially detached from the surface. This shows that the peptide leading to the characteristic peak colocalizing with the bottom of the cell is transported through the cell layer and sticks to the surface after being transported fully across the cell barrier.

### 3. Discussion

Here we investigated the transport of sCT modified with two lipid side chains at position 20 and 26. While most of the literature focuses on single lipidation of peptides [12,44–48] and cyclization [49], less has been done with double lipidations with side chains [50–53]. Single lipidation increases transport, and the general mechanism for this is the increase of the drugs lipophilicity. Lipidation has been shown to reduce degradation in the case of for example insulin [23], but also of sCT [50,53]. In the case of double lipidation, the two side chains are thought to orient the peptide molecule to the lipid bilayer. It has been shown to increase the interaction with the cell membrane [52]. We showed that double lipidation improves transport, that longer side chains also do and that the endocytic pathway is involved depending on the lipidation. We did this by a fast assay based on live-cell imaging with single cell kinetic information. Single lipidation of sCT at the N-terminus with a C8 lipid chain has previously been shown to increase the overall transport through Caco-2 cells by 10-fold [12]. We saw here that double lipidation using shorter lipid chains also increases transport compared to single lipidation.

The increased interaction of lipidated peptides with the membrane leads to transport; however there are several hypotheses for the mechanism involved. In one scenario, the association of the peptide with the lipid membrane is an equilibrium (partition) such that the peptide stochastically crosses the membrane and dissociates on the other side. This exchange across the lipid membrane should occur on both sides of the cells. In this scenario, the overall transport of the lipidated peptide occurs transcellularly, and we thus expect to detect a diffuse signal inside the cytosol in our assay. In another scenario, the lipidated peptide associates with the lipid membrane and is transported towards the basolateral of the cells by diffusion along the lipid membrane. In both cases, we expect to measure a signal for the peptide partitioning on the cell membrane; the peptide signal should colocalize with the cell membrane on the apical and basolateral sides. Alternatively, the peptide is transported via endocytosis, and in this case, we expect the peptide signal to appear as puncta in the cells.

At first glance, real time fluorescence confocal imaging of a fluorescently labelled peptide could easily pinpoint the main fate of the peptide in Caco-2 cells and lead to a mechanistic understanding of the transport. However, current platforms used for differentiating cells are not readily amenable to high magnification live-cell imaging and in particular they are not readily applicable to advanced imaging modalities that could ultimately provide single molecule tracking for mechanistic studies. Additionally, even with high magnification confocal microscopy, the axial resolution complicates the quantitative analysis of the fluorescence signal when transport occurs through cells in the direction of the imaging i.e. axially.

Here we establish a cellular model that requires only a short cell cultivation period which has the advantage to be suitable for high NA live-cell imaging, but at the cost of a reduced in vivo translatability. The short-term culture leads to a low thickness of the cytoplasm compared to fully polarized Caco-2 cells that are more cuboidal. This is somewhat challenging the resolution of the different compartments of the cellular model however we can use a physical model of the cell layer that is suitable for axial PSF deconvolution of the intensity profile through the cell layer. A physical model combined with PSF deconvolution allows us

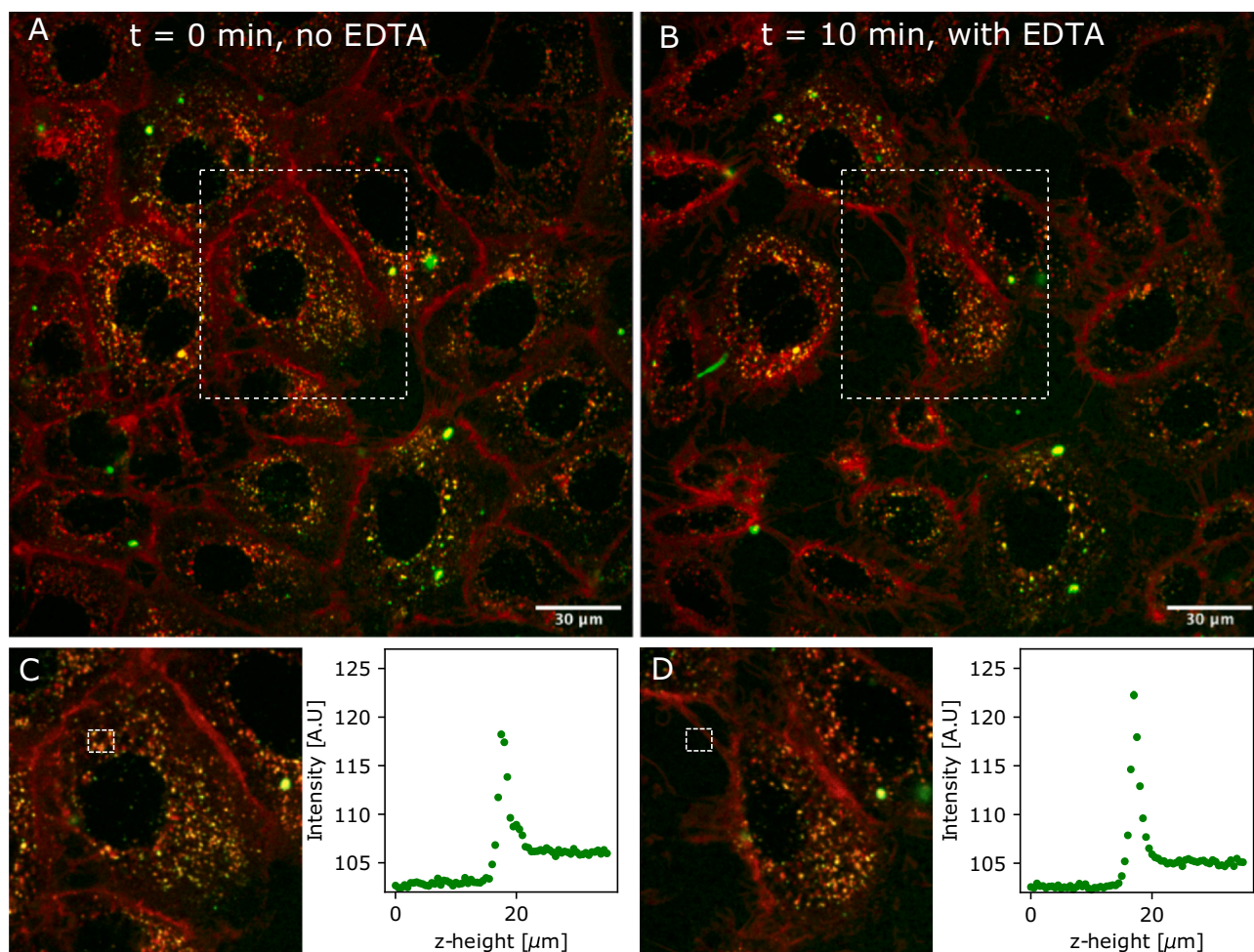


**Fig. 6.** sCT(C8/C8) signal persist after cells are exposed to EDTA. A) Maximum projection image before adding EDTA. B) Same FOV after 10 min incubation with 1.5  $\mu\text{M}$  EDTA. C) Cropped image of the cell of interest and axial intensity profile in the ROI at  $t = 0$  and D) at  $t = 10$  min after cell has detached from the surface.

to extract the individual contributions of the solution, the cytosol, and the cell bottom membrane to the overall intensity profile.

Cells are grown for 2 days, considerably shorter than the traditional 21 days seen for most Transwell systems. Hence, we validated the applicability of our system for studying cross-barrier peptide transport using a positive control (TAT) and negative controls (Dextran and Lucifer Yellow). Our results confirm that the barrier formed by 2-days old cells is tight, thus, our model can quantify the cytosolic peptide content (Fig. 3) and the amount of peptide that ends up colocalized with the bottom of the cells (Figs. 3 and 4). We compare our minimal model to a cell model with fully polarized cells. Polarized Caco-2 cells have a lower endocytic activity and form a thicker cell layer, similarly to in vivo intestinal barrier cells. Most cellular model formats leading to polarized cells are inadequate for high NA imaging. Here we used a microfluidic platform to grow such cells. This assay is more time consuming and costly than the assay presented here however, it has the advantage that it allows high NA imaging so we can readily apply our imaging conditions and analysis to a cell model that has fully polarized cells [36].

Our physical model of the cell assumes that 1) the cytosol is a medium with a uniform peptide intensity 2) separated by a flat and thin membrane at the bottom and the top. For this model to be valid, we arbitrarily choose to sample the axial intensity profile through the cytosol, away from the nucleus. By doing this we neglect the non-uniform peptide signal that occurs when peptides are accumulating in puncta-like structures. Puncta-like peptide signal is readily seen on the images of cells incubated with the sCT(C8/C8) analog and in the axial intensity profile sampled over the nucleus (Fig. S8). In this case the

physical model for deconvolution must be modified to include a PSF-like peak colocalizing with the top of the cell seen on the peptide channel. This peak originates from the endosome signal that surround the nucleus and colocalizes with the top membrane when the intensity is sampled over the nucleus, but is absent when the intensity is sampled away from the nucleus. This agrees with what we see in the images of the TAT-FITC and the sCT(C8/C8) where the endosomes are gathered around the nucleus (Fig. S9 and S10). This effect makes the interpretation of the peptide signal peak at the bottom of the cell more difficult and so, we opted to sample through the cytosol to quantify the transport of the lipidated peptides in the cytosol without the influence of the puncta-like structures. Conversely, most of the PSF deconvolution work done in the context of cellular transport studies is focusing on tracking of puncta-like signals and colocalization with organelles [54–56]. Here instead we focus on measuring the diffuse peptide signal that is in the cytosol and the peptide signal collocated at the basolateral side of the cell layer.

We established a live-cell imaging-based assay to quantify the transport of peptides through Caco-2 cells. Beyond the advantages highlighted here, a live-cell imaging assay offers a perspective to imaging modalities that can provide single molecule resolution. The price to pay is the modification with a label that can modify the properties of the peptide. Here we make sure to minimize this influence and compare sCT analogues keeping all other artifacts equal. We chose a fluorophore known to have little interaction with cell membranes [33]. We choose to attach the fluorophore to the N-terminus of the peptide and not to the lipid side chains. Lipidation of peptides has been shown to reduce degradation of peptides [50,53,57]. Degradation of the peptide is thus

expected to be worse for the native sCT and thus lead to an increase of transport of the label alone or fragments of the sCT in the case of the native sCT. This is not what we observe.

In our study we also aim to gain some insight into how the lipidation of sCT affects the transport mechanisms. Remarkably, none of the sCT analogs showed an increase of peptide signal in the cytosol, as opposed to what the addition of TAT showed (Fig. 3G). This implies that concomitant quantification of the signal in the cytosol and at the bottom of the cell can be used to address the transport mechanisms of the sCT analogs. Indeed, this suggests that the sCT analogs are either 1) taken up by endosomal carriers and transported inside organelles of a vesicular pathway from the apical- to the basolateral cell side, or 2) that the peptides interact with the membrane and then equilibrate by diffusion over the cell membrane hereby reaching the basolateral side. Moreover, transport is inhibited fully or partially by lowering the temperature (Fig. 5). This is expected as temperature reduces the kinetics of all transport pathways, whether endocytosis or diffusion in the membrane. In contrast, addition of Dynasore that is a specific endocytosis inhibitor affects primarily the accumulation of sCT(C8/C8) and sCT(C0/C0) while it is not affecting the transport of sCT(C4/C4). The reduction in transport is most significant for the sCT(C8/C8) and this strongly suggests that the predominant transport mechanism is one of the endocytotic pathways inhibited by Dynasore, that is, Clathrin or Caveolin-mediated. Also, the intensity of the sCT(C8/C8) signal under the cells exceeds significantly that of the peptide solution itself, suggesting that the accumulation results from an active transport, such as endocytosis, and subsequent accumulation in a sink probably being the cellular junk below the cell. Qualitatively this also agrees with what is seen in the raw imaging data of cells incubated with the peptides: sCT(C0/C0) and sCT(C4/C4) show little to no signs of peptide in endosomes (Fig. S10 A-D), but sCT(C8/C8) shows many puncta-like structures, which we interpret as vesicular structures (Fig. S10 E-F).

Finally, the addition of the endocytosis inhibitor does not completely suppress the accumulation of peptides below the cells for sCT(C8/C8), suggesting that an additional mechanism could be at play, for example, association of the lipidated peptide to the membrane followed by diffusion along the lipid membrane. To assess this, our assay could be adapted for other fluorescence imaging modalities such as tracking of single molecules using single molecule microscopy.

### 3.1. Similarity with other modifications and transport studies

It was previously shown, using temperature measurements and the Transwell system, that the transport of native sCT occurs primarily through passive diffusion as transcellular transport in a Caco-2 cell layer [58]. Our data show that that addition of two 8-carbon lipid chains significantly increases the overall transport. The general effect of the addition of hydrophobic groups fits with what others have shown using the Transwell systems; the overall transport of sCT through a Caco-2 monolayer can be increased by biotinylation [59], deoxycholic acid [60] or proliposomes [61]. In particular, it was shown that the addition of biotin to sCT changes the uptake mechanism to a carrier mediated transport through the sodium-dependent multivitamin transporter systems [59] but also increases the passive diffusion [62,63]. Here we observe a change of the transport pattern of double-lipidated peptides, and also our imaging assay suggests that the length of the lipid side chains grafted on sCT modifies the cellular transport.

### 3.2. Applicability of the assay

Our study demonstrates the potential of a live-cell imaging assay that can resolve the transport kinetics for the same individual cells and thus circumvent the artefacts of analyzing end point measurements for different sets of cells as is done on a platform that does not allow real-time high magnification imaging. Additionally, the live-cell imaging has the ability of multiplexing experiments via the automation of

imaging for multiple fields of view.

Moreover, in our assay, we can gain some mechanistic understanding by characterizing not only the quantitative information of the peptide transported through the cell layer but also the qualitative information provided by live-cell imaging of short-time grown cells.

However, our imaging assay is fast partly because it is based on short-term cell culture, which cannot recapitulate all functions of the gut epithelial. For this reason the 21-days cell cultures and in vivo assays are still preferred in the industry. Nevertheless, we believe that early-stage imaging assays can offer efficient mechanistic insights, although in a minimalistic biological environment, which could help further designing new modifications of peptide candidates for orally administered drugs before engaging in more biological complex, time consuming and expensive assays like single molecule tracking efforts in tissue samples or animal studies.

## 4. Conclusion

In conclusion, we showed that double lipidation of salmon calcitonin with lipid chains can alter the amount of peptide transported across a Caco-2 monolayer. Furthermore, we showed that the underlying transport mechanism is affected by the length of the lipid chains. We achieved this by applying a model of the cellular layer to deconvolute the axial intensity profile and access the peptide signal contribution in the solution, the cytosol, and the bottom membrane of the cells. This model allowed us to interpret the fluorescence signal obtained by confocal imaging across a cell layer as thin as the axial resolution of our microscope. This model further showed that we get leak-tight barriers by utilizing a simple cell model where cells are only grown for two days. These results showed that lipidation of peptides may increase their bioavailability. Still, more importantly, we provide a model and a tool for an easy and quantitative experimental setup, which will enhance the knowledge of how to increase the bioavailability of biopharmaceuticals administered orally.

## 5. Materials and methods

### 5.1. Cell culture

The Caco-2 cells were kept in a T75 culture flask (Nunc EasYFlask 75 cm<sup>2</sup> Cat. Nr. 156,472) with 12 mL Minimum Essential Medium (MEM) with 10% FBS, 1% L-glutamine, 1% non-essential amino acids and 1% Penicillin/streptomycin. The cells were placed in an incubator at 37 °C with 95% O<sub>2</sub>, 5% CO<sub>2</sub>, and 5% humidity. The cells were grown to approximately 90% confluency before splitting for the transport experiment.

### 5.2. Synthesis of salmon calcitonin

#### 5.2.1. Abbreviations

DMF, *N,N*-dimethylformamide; DIPEA, *N,N*-diisopropylethylamine; TFA, trifluoroacetic acid; DIC, diisopropylcarbodiimide; Oxyma, ethyl cyanohydroxyiminoacetate; TIPS, triisopropylsilane; HFIP, hexafluoroisopropanol.

### 5.3. Materials

Fmoc-protected amino acids, oxyma and DIC were purchased from Iris-Biotech. The resin was purchased from Rapp Polymere. Solvents and all other reagents were purchased from Sigma Aldrich.

Special Fmoc amino acids: Fmoc-Oc<sub>2</sub>O-OH (Fluorenylmethoxycarbonyl-amino-3,6-dioxaoctanoic acid), Fmoc-*L*-Leu-*L*-Ser[PSI(*Me*, *Me*)Pro]-OH, Fmoc-*L*-Glu-OtBu, Fmoc-*L*-Asp-OtBu.

#### 5.4. Synthesis of lipidated amino acids

Fmoc-L-AA-OtBu (AA = Glu or Asp, 4.86 mmol, 1 eq.) was dissolved in dichloromethane (100 mL). PyBOP (2.53 g, 4.86 mmol, 1 eq.), DIPEA (1.88 g, 2.54 mL, 14.6 mmol, 3 eq.) and amino-lipid (butylamine or octylamine) (5.35 mmol, 1.1 eq.) were added, and the reaction mixture was stirred overnight. The mixture was evaporated in vacuo, re-dissolved in EtOAc, washed with 1 M KHSO<sub>4</sub> (2×), sat. NaHCO<sub>3</sub> (2×), brine (2×), dried over MgSO<sub>4</sub>, filtered, and evaporated to dryness in vacuo.

The ester-product was re-dissolved in DCM (30 mL). TFA (15 mL) was added, stirred for 1 h, and evaporated in vacuo. The product was re-dissolved in DMF (5 mL) and precipitated with water. The precipitate was centrifuged (5 min, 6000 rpm), and the supernatant was decanted. The product was lyophilized to yield colourless powders. The correct masses were identified using MALDI-TOF MS.

#### 5.5. Solid phase peptide synthesis

Peptides were synthesized on a Biotage Initiator + Alstra microwave-assisted peptide synthesizer in 10 mL fritted syringes on a 0.05 mmol scale. Tentagel S-RAM resin was used (0.23 mmol/g). Fmoc-deprotection was performed by adding 5 mL of deprotection solution (20% piperidine in DMF, 0.1 M Oxyma) to the resin at 75 °C for 30 s. The resin was drained and washed once with DMF (5 mL). Another portion of deprotection solution (5 mL) was added and heated to 75 °C for 2 min. Next, the resin was drained and washed five times with DMF (5 mL). Coupling of amino acids was performed by adding amino acid solution (4 eq. of Fmoc-L-AA-OH, 4 eq. Oxyma in DMF, 0.3 M concentration), DIC solution (5 eq., 2 M DIC in DMF) and heating the mixture to 75 °C for 5 min. The solution was drained and the resin was washed once with 5 mL DMF. The coupling was repeated. After the second coupling the resin was washed 4 times with 5 mL DMF. Extended coupling times were applied for Fmoc-Arg(Pbf)-OH, Fmoc-L-Leu-L-Ser[PSI(Me, Me)Pro]-OH and the lipidated amino acids Fmoc-L-Asp(C4)-OH, Fmoc-L-Asp(C8)-OH, Fmoc-L-Glu(C4) and Fmoc-L-Glu(C8)-OH. These amino acids were coupled at room temperature for 25 min followed by 75 °C for 5 min. The resin was drained, washed 4 times with DMF (5 mL) and the coupling was repeated. Fmoc-removal on Asp residues was performed with 5% piperidine rather than 20%.

#### 5.6. Formation of disulfide on resin

After coupling of Fmoc-Oc<sub>2</sub>O-OH, the resin was washed five times with DCM (5 mL). An iodine solution (5 mL; 1:4 HFIP/1% I<sub>2</sub> in DCM) was added to the resin, shaken for exactly 2 min, filtered, and washed once with a 1:1 HFIP/DCM solution. The resin was then left to shake for 15 min with a 1:1 HFIP/DCM solution. The solution was drained, and the resin was washed five times with DCM and five times with DMF. Next, Fmoc was removed by adding 20% piperidine, 0.1% Oxyma in DMF (5 mL), and the tube was shaken for 2 × 20 min. The resin was washed with DMF, DCM, DMF, DCM, *i*-PrOH, DCM, and Et<sub>2</sub>O.

#### 5.7. Atto coupling, peptide cleavage, purification and analysis

Atto488 (5 mg, 5.1 μmol), dry DIPEA (5 eq., 20.4 μmol, 3.55 μL) were dissolved in dry DMF (200 μL) and added to 45 mg resin (approx. 5.7 μmol). The tube was shaken overnight in the dark. The resin was washed 5 times with DMF (5 mL), 5 times with DCM (5 mL) and air-dried. The resin was treated with cleavage cocktail (0.6 mL; 90% TFA, 5% water, 5% TIPS) for 240 min. The crude peptide was precipitated in cold diethylether, centrifuged, and decanted. The residue was air-dried and re-dissolved in 20% MeCN in MQ. The crude peptide was purified on a Dionex Ultimate 3000 system equipped with a RQ variable wavelength detector and an automated fraction collector using a Phenomenex, Gemini NX 5u, C18, 110 Å, AXIA, 250 mm × 21 mm column at a 20 mL/

min flowrate. RP-HPLC gradients were run using a solvent system consisting of solution A (H<sub>2</sub>O + 0.1% TFA) and B (MeCN + 0.1% TFA). Pure fractions were combined and lyophilized. Peptides were analyzed on a Shimadzu NexeraX2 reverse-phase HPLC (RP-HPLC) system equipped with Shimadzu LC-30 CE pumps, a Shimadzu SIL-30 AC autosampler, a CTO-20 AC column oven and a Shimadzu PDA detector (monitoring at 214 nm, 280 nm and 492 nm) using a Waters XBridge BEH C18, 2.5 μm 3.0x150mm XP Column at a flow rate of 0.5 mL/min. RP-HPLC gradients were run using a solvent system consisting of solution A (5% MeCN in H<sub>2</sub>O + 0.1% TFA) and B (MeCN + 0.1% TFA). Mass analysis was performed with autoflex-MALDI-TOF (Bruker) or UHPLC-Microtof-Q III LC-MS system (Bruker).

#### 5.8. Cell seeding

At 90% confluency, the medium in the T75 flask was removed, and the cells were washed with 10 mL of a cell suitable PBS (D8537-500ML Sigma) preheated to 37 degrees. The PBS was removed and replaced with 1 mL trypsin/EDTA and placed in the incubator at 37 °C with 95% O<sub>2</sub>, 5% CO<sub>2</sub>, and 5% humidity for approximately 5 min or until the cells were detached from the surface of the flask. The trypsin/EDTA solution was deactivated by adding 9 mL cell medium. The cell density per mL was found using a NucleoCounter. 30,000 cells were seeded per well and grown for two days.

#### 5.9. Cell staining

Cells were stained for 30 min with 1 μg/mL Hoechst 33342 (H1399, Thermo Fisher, 10 μg/mL) in Fluorobrite (ThermoFisher, A1896701). After staining the cells were washed once in clean fluorobrite. After staining with fluorobrite, the cells were labelled with CellMask DeepRed plasma membrane stain (ThermoFisher, C10046) diluted 2000 times for approximately 10 min. After the staining, the cells were washed in fluorobrite 3 times.

#### 5.10. Imaging

For the transport studies, a confocal spinning disk (inverted Nikon Ti2 with Yokogawa CSU-W1 SD system with 50 μm pinholes) with a 60 × 1.4 NA oil objective (CFI Plan Apochromat Lambda 60× Oil).

was used. The microscope was connected to a heater and CO<sub>2</sub> to maintain favorable conditions for the cells. The heater was set to 37 °C, and the CO<sub>2</sub> was set to 5%. A water reservoir was also present to maintain humidity while imaging. Three different lasers were used. 405 nm laser at 8% to excite the nucleus stained with Hoechst. A 488 nm laser at 10% was used to excite the peptides. A 638 nm laser was used to excite the CellMask DeepRed, labeling the membrane of the cells. A quadband emission filter was used to capture the emitted light for faster acquisition with a sCMOS (Photometrics Prime 95B) camera.

Several fields of views (FOVs) at 1200 × 1200 pixels (180 nm × 180 nm pixel size) were picked out using the mark and find positioning plugin in the Nikon software. After all the FOVs were picked, a z-stack was taken of all the FOVs marked. The z-stack consisted of 71 steps, where each step was 0.5 μm. After taking the z-stack, the peptide was added carefully. After adding the peptide, all FOVs were corrected back to the original position in *x*, *y*, and *z* if needed. After the correction, a time series was set up to run for 4 h, imaging every FOV with a z-stack every 40 min yielding seven time points.

#### 5.11. Point spread function measurement

The width of the point spread function (PSF) is dependent on many parameters of the confocal microscope, including the excitation and emission wavelength. Hence, we pragmatically measure the axial PSF for the 488 nm and the 638 nm excitation of our spinning disc confocal microscope. To this end, 100 nm fluorescent polymer beads

(ThermoFisher, T7279) were used. The beads were small enough to be considered point sources due to the diffraction limit and have the advantage that they can be imaged at four different wavelengths. A z-stack was taken to estimate the PSF in the z-direction. The axial intensity profile essentially shows the axial PSF as seen in Supplementary Fig. S1. The PSF is approximated with the sum of two Gaussians, as seen in the equation below.

$$f(z) = \frac{a}{\sqrt{2\pi}} \left[ \frac{c}{\sigma} e^{-\left(\frac{z-\mu}{\sigma\sqrt{2}}\right)^2} + \frac{1-c}{d\sigma} e^{-\left(\frac{z-\mu-\mu_{\text{shift}}}{d\sigma\sqrt{2}}\right)^2} \right] + b$$

$$= \frac{a}{\sqrt{2\pi}} \left( \frac{c}{\sigma} e^{-[A(z,\mu)]^2} + \frac{1-c}{d\sigma} e^{-[B(z,\mu)]^2} \right) + b.$$

One gaussian is high and slim, whereas the second one is low and wide. This means that the width  $\sigma$  of the two Gaussians are not the same. To express the double Gaussian with a single width  $\sigma$ , a scaling factor is introduced to get the width of the low and wide gaussian. This factor is called  $d$  and is defined as:  $d = \sigma_{\text{wide}}/\sigma_{\text{narrow}}$ . Furthermore, the center position  $\mu$  of the two Gaussians is shifted compared to one another. Hence, a shift parameter  $\mu_{\text{shift}}$  is introduced and is defined as the difference between the two positions. The factor  $c$  is a weight determining how much of each of the gaussian should be represented in the sum of the Gaussians. For convenience we define  $A$  and  $B$  two functions of  $z$  and  $\mu$ .

The overall shape of the fit to the axial PSF for the 488 nm and 638 nm excitation was used to deconvolute the axial intensity profiles through the cells.

### 5.12. Deconvolution of the axial intensity profiles

After acquiring one three-colour confocal stack per FOV, each FOV was analyzed and processed individually. A  $10 \times 10$  pixels region of interest (ROI) was picked out for each eligible cell. Typically, the ROI was close to the nuclei but not in the nuclei. After picking out the ROIs, the intensity signal in the ROI was in each z-plane of the z-stack for each colour. The intensity from the blue channel was used to verify that the ROI was not placed inside the nucleus. Despite this, the intensity trace from the nuclei channel can still show a small (4–5 intensity units) increase when the ROI is inside the cell as seen in Fig. 1C left panel.

We first fit the axial intensity profile from the membrane channel to locate the cell's lower and upper membrane layers. We select the ROIs so that the membrane can be modeled by an infinitely thin plane; thus the intensity profile is fitted with two axial PSFs and a constant background:

$$f(z) = \frac{a_1}{\sqrt{2\pi}} \left( \frac{c}{\sigma} e^{-[A(z,\mu_1)]^2} + \frac{1-c}{d\sigma} e^{-[B(z,\mu_1)]^2} \right)$$

$$+ \frac{a_2}{\sqrt{2\pi}} \left( \frac{c}{\sigma} e^{-[A(z,\mu_2)]^2} + \frac{1-c}{d\sigma} e^{-[B(z,\mu_2)]^2} \right) + b.$$

Five parameters are fitted;  $a_1$ , the amplitude of the PSF describing the lower cell membrane,  $a_2$  describing the amplitude of the second PSF,  $\mu_1$  the position of the lower membrane,  $\mu_2$  the position of the upper membrane, and  $b$  the background signal. The remaining parameters in the function are found experimentally from the PSF at the 638 nm excitation.

Next, the axial intensity signal from the peptide channel is used to quantify peptide signal in the solution, the cytosol, and colocalized with the bottom membrane. The contribution from the solution is described by a step function convoluted with the axial PSF. Similarly the cytosol contribution is defined by two step functions convoluted with the PSF. The signal colocalized with the bottom membrane is modeled by the PSF at 488 nm excitation. The function describing the intensity profile of the peptide channel is thus described by:

$$f(z) = \frac{a_1}{2} [c(1 + \text{erf}[A(z,\mu_1)]) + (1-c)(1 + \text{erf}[B(z,\mu_1)])]$$

$$+ \frac{a_2}{2} [c(1 + \text{erf}[A(z,\mu_2)]) + (1-c)(1 + \text{erf}[B(z,\mu_2)])]$$

$$+ \frac{a_3}{\sqrt{2\pi}} \left[ \frac{c}{\sigma} e^{-[A(z,\mu_1)]^2} + \frac{1-c}{d\sigma} e^{-[B(z,\mu_1)]^2} \right] + b.$$

Here,  $a_1$  is the amplitude of the first error function, which describes the plateau in the cell's cytosol. Parameter  $a_2$  is the amplitude of the second error function. The sum of  $a_1$  and  $a_2$  represents the plateau in the solution. Parameter  $a_3$  is the amplitude of the peak that colocalizes with the bottom membrane of the cell and  $b$  is the background intensity. All other parameters in the function are known from prior fitting of the membrane signal (the positions of the membranes) and of the shape of the axial PSF at the 488 nm excitation. From the fit we obtain the fitted values of  $a_1$ ,  $a_2$  and  $a_3$ .

### CRediT authorship contribution statement

**Adam Coln Hundahl:** Investigation, Writing – original draft. **Arjen Weller:** Investigation. **Jannik Bruun Larsen:** Conceptualization, Supervision. **Claudia U. Hjørringgaard:** Investigation. **Morten B. Hansen:** Investigation. **Ann-Kathrin Müндler:** Investigation. **Astrid Knuhtsen:** Investigation. **Kasper Kristensen:** Investigation. **Eva C. Arnspang:** Supervision. **Thomas Lars Andresen:** Conceptualization. **Kim I. Mortensen:** Conceptualization, Supervision. **Rodolphe Marie:** Conceptualization, Supervision.

### Data availability

Data will be made available on request.

### Acknowledgements

This work was supported by the Novo Nordisk Foundation (grant no. NNF16OC0022166 to TLA). We thank DaMBIC – Danish Molecular Bioimaging Center at the Southern Denmark University for access to microscopes.

### Appendix A. Supplementary data

Supplementary information to this article can be found online at <https://doi.org/10.1016/j.jconrel.2023.01.066>.

### References

- [1] S. Mitragotri, P.A. Burke, R. Langer, Overcoming the challenges in administering biopharmaceuticals: formulation and delivery strategies, *Nat. Rev. Drug Discov.* 13 (9) (2014) 655–672, <https://doi.org/10.1038/nrd4363>.
- [2] P. Hinderliter, S.A. Saghir, Pharmacokinetics. *Encyclopedia of Toxicology: Third Edition* 3, 2014, pp. 849–855, <https://doi.org/10.1016/B978-0-12-386454-3.000419-X>.
- [3] M.W. Tibbitt, J.E. Dahلمان, R. Langer, *Emerging Frontiers in Drug Delivery*, J. Am. Chem. Soc. 138 (3) (2016) 704–717, <https://doi.org/10.1021/jacs.5b09974>.
- [4] A.C. Anselmo, Y. Gokarn, S. Mitragotri, Non-invasive delivery strategies for biologics, *Nat. Rev. Drug Discov.* 18 (1) (2018) 19–40, <https://doi.org/10.1038/nrd.2018.183>.
- [5] R. Ismail, I. Csóka, Novel strategies in the oral delivery of antidiabetic peptide drugs – insulin, GLP 1 and its analogs, *Eur. J. Pharm. Biopharm.* 115 (2017) 257–267, <https://doi.org/10.1016/j.ejpb.2017.03.015>.
- [6] J. Renukuntla, A.D. Vadlapudi, A. Patel, S.H.S. Boddu, A.K. Mitra, Approaches for enhancing oral bioavailability of peptides and proteins, *Int. J. Pharm.* 447 (1–2) (2013) 75–93, <https://doi.org/10.1016/j.ijpharm.2013.02.030>.
- [7] D. Manzanera, V. Ceña, Endocytosis: the nanoparticle and submicron nanocompounds gateway into the cell, *Pharmaceutics* 12 (4) (2020) 1–22, <https://doi.org/10.3390/pharmaceutics12040371>.
- [8] D.J. Drucker, Advances in oral peptide therapeutics, *Nat. Rev. Drug Discov.* 19 (4) (2020) 277–289, <https://doi.org/10.1038/s41573-019-0053-0>.
- [9] S. Verma, U.K. Goand, A. Husain, R.A. Katekar, R. Garg, J.R. Gayen, Challenges of peptide and protein drug delivery by oral route: current strategies to improve the bioavailability, *Drug Dev. Res.* (2021), <https://doi.org/10.1002/ddr.21832>.
- [10] R.G. Diedrichsen, S. Harloff-Helleberg, U. Werner, M. Besenius, E. Leberer, M. Kristensen, H.M. Nielsen, Revealing the importance of carrier-cargo association

- in delivery of insulin and lipidated insulin, *J. Control. Release* 338 (July) (2021) 8–21, <https://doi.org/10.1016/j.jconrel.2021.07.030>.
- [11] R. Menacho-Melgar, J.S. Decker, J.N. Hennigan, M.D. Lynch, A review of lipidation in the development of advanced protein and peptide therapeutics, *J. Control. Release* 295 (2019) 1–12, <https://doi.org/10.1016/j.jconrel.2018.12.032>.
- [12] S. Trier, L. Linderoth, S. Bjerregaard, H.M. Strauss, U.L. Rahbek, T.L. Andresen, Acylation of salmon calcitonin modulates in vitro intestinal peptide flux through membrane permeability enhancement, *Eur. J. Pharm. Biopharm.* 96 (2015) 329–337, <https://doi.org/10.1016/j.ejpb.2015.09.001>.
- [13] I. Behrens, P. Stenberg, P. Artursson, T. Kissel, Transport of lipophilic drug molecules in a new mucus-secreting cell culture model based on HT29-MTX cells, *Pharm. Res.* 18 (8) (2001) 1138–1145, <https://doi.org/10.1023/A:1010974909998>.
- [14] Y. Yang, Y. Zhao, A. Yu, D. Sun, L.X. Yu, Oral drug absorption: evaluation and prediction, in: *Developing Solid Oral Dosage Forms: Pharmaceutical Theory and Practice: Second Edition* 331–354, 2017, <https://doi.org/10.1016/B978-0-12-802447-8.00012-1>.
- [15] D. Birch, R.G. Diedrichsen, P.C. Christophersen, H. Mu, H.M. Nielsen, Evaluation of drug permeation under fed state conditions using mucus-covered Caco-2 cell epithelium, *Eur. J. Pharm. Sci.* 118 (January) (2018) 144–153, <https://doi.org/10.1016/j.ejps.2018.02.032>.
- [16] V. Gupta, N. Doshi, S. Mitragotri, Permeation of insulin, calcitonin and Exenatide across Caco-2 monolayers: measurement using a rapid, 3-day system, *PLoS One* 8 (2) (2013), <https://doi.org/10.1371/journal.pone.0057136>.
- [17] J. Capoulade, M. Wachsmuth, L. Hufnagel, M. Knop, Quantitative fluorescence imaging of protein diffusion and interaction in living cells, *Nat. Biotechnol.* 29 (9) (2011) 835–839, <https://doi.org/10.1038/nbt.1928>.
- [18] D.J. Brayden, J. Gleeson, E.G. Walsh, A head-to-head multi-parametric high content analysis of a series of medium chain fatty acid intestinal permeation enhancers in Caco-2 cells, *Eur. J. Pharm. Biopharm.* 88 (3) (2014) 830–839, <https://doi.org/10.1016/j.ejpb.2014.10.008>.
- [19] R. Brock, The uptake of arginine-rich cell-penetrating peptides: putting the puzzle together, *Bioconjug. Chem.* 25 (5) (2014) 863–868, <https://doi.org/10.1021/bc500017t>.
- [20] T.B. Potocky, A.K. Menon, S.H. Gellman, Cytoplasmic and nuclear delivery of a TAT-derived peptide and a  $\beta$ -peptide after endocytic uptake into HeLa cells, *J. Biol. Chem.* 278 (50) (2003) 50188–50194, <https://doi.org/10.1074/jbc.M308719200>.
- [21] T. Kowada, H. Maeda, K. Kikuchi, BODIPY-based probes for the fluorescence imaging of biomolecules in living cells, *Chem. Soc. Rev.* 44 (14) (2015) 4953–4972, <https://doi.org/10.1039/c5cs00030k>.
- [22] S. Zhang, C. Ma, M. Chalfie, Combinatorial marking of cells and organelles with reconstituted fluorescent proteins, *Cell* 119 (1) (2004) 137–144, <https://doi.org/10.1016/j.cell.2004.09.012>.
- [23] C. Thompson, W.P. Cheng, P. Gadad, K. Skene, M. Smith, G. Smith, R. Knott, Uptake and transport of novel amphiphilic polyelectrolyte-insulin nanocomplexes by caco-2 cells-towards oral insulin, *Pharm. Res.* 28 (4) (2011) 886–896, <https://doi.org/10.1007/s11095-010-0345-x>.
- [24] C. Zimmermann, S. Rudloff, G. Lochnit, S. Arampatzi, W. Maison, K.P. Zimmer, Epithelial transport of immunogenic and toxic gliadin peptides in vitro, *PLoS One* 9 (11) (2014) 1–17, <https://doi.org/10.1371/journal.pone.0113932>.
- [25] N. Vtyurina, C. Åberg, A. Salvati, Imaging of nanoparticle uptake and kinetics of intracellular trafficking in individual cells, *Nanoscale* 13 (23) (2021) 10436–10446, <https://doi.org/10.1039/d1nr00901j>.
- [26] J.A. Conchello, J.W. Lichtman, Optical sectioning microscopy, *Nat. Methods* 2 (12) (2005) 920–931, <https://doi.org/10.1038/nmeth815>.
- [27] J.A. Helmuth, C.J. Burckhardt, U.F. Greber, I.F. Sbalzarini, Shape reconstruction of subcellular structures from live cell fluorescence microscopy images, *J. Struct. Biol.* 167 (1) (2009) 1–10, <https://doi.org/10.1016/j.jsb.2009.03.017>.
- [28] E.M. Smith, J. Hennen, Y. Chen, J.D. Mueller, Z-scan fluorescence profile deconvolution of cytosolic and membrane-associated protein populations, *Anal. Biochem.* 480 (2015) 11–20, <https://doi.org/10.1016/j.ab.2015.03.030>.
- [29] S. Chen, F. Guo, T. Deng, S. Zhu, W. Liu, H. Zhong, Z. Deng, Eudragit S100-coated chitosan nanoparticles co-loading tat for enhanced Oral Colon absorption of insulin, *AAPS PharmSciTech* 18 (4) (2017) 1277–1287, <https://doi.org/10.1208/s12249-016-0594-z>.
- [30] A. Betanzos, D. Zanatta, C. Bañuelos, E. Hernández-Nava, P. Cuellar, E. Orozco, Epithelial cells expressing EHADH, an Entamoeba histolytica Adhesin, exhibit increased tight junction proteins, *Front. Cell. Infect. Microbiol.* 8 (September) (2018) 1–17, <https://doi.org/10.3389/fcimb.2018.00340>.
- [31] C. Rousou, J. De Maar, B. Qiu, K. Van Der Wurff-jacobs, M. Ruponen, A. Urtili, R. Deckers, The Effect of Microbubble-Assisted Ultrasound on Molecular Permeability across Cell Barriers, 2022.
- [32] Sofie Fogh Hedegaard, Mohammed Sobhi Derbas, Tania Kjellerup Lind, Marina Robertnova Kasimova, Malene Vinther Christensen, Maria Hotoft Michaelsen, Richard A. Campbell, et al., Fluorophore labeling of a cell-penetrating peptide significantly alters the mode and degree of biomembrane interaction, *Sci. Rep.* 8 (1) (2018) 6327, <https://doi.org/10.1038/s41598-018-24154-z>.
- [33] L.D. Hughes, R.J. Rawle, S.G. Boxer, Choose your label wisely: water-soluble fluorophores often interact with lipid bilayers, *PLoS One* 9 (2) (2014), e87649, <https://doi.org/10.1371/journal.pone.0087649>.
- [34] S. Yamashita, K. Konishi, Y. Yamazaki, Y. Taki, T. Sakane, H. Sezaki, Y. Furiyama, New and better protocols for a short-term Caco-2 cell culture system, *J. Pharm. Sci.* 91 (3) (2002) 669–679, <https://doi.org/10.1002/jps.10050>.
- [35] S.J. Trietsch, E. Naumovska, D. Kurek, M.C. Setyawati, M.K. Vormann, K. J. Wilschut, P. Vulto, Membrane-free culture and real-time barrier integrity assessment of perfused intestinal epithelium tubes, *Nat. Commun.* 8 (1) (2017) 1–7, <https://doi.org/10.1038/s41467-017-00259-3>.
- [36] A. Weller, M.B. Hansen, R. Marie, A.C. Hundahl, C. Hempel, P.J. Kempen, H. L. Frandsen, L. Parhamifar, J.B. Larsen, T.L. Andresen, Quantifying the transport of biologics across intestinal barrier models in real-time by fluorescent imaging, *Front. Bioeng. Biotechnol.* (2022), <https://doi.org/10.3389/fbioe.2022.965200>.
- [37] W.J. Conover, R.L. Iman, On Multiple-comparisons Procedures, Los Alamos National Lab. (LANL), Los Alamos, NM (United States), 1979, <https://doi.org/10.1177/002205741508200834>.
- [38] B.J. Iacopetta, E.H. Morgan, The kinetics of transferrin endocytosis and iron uptake from transferrin in rabbit reticulocytes, *J. Biol. Chem.* 258 (15) (1983) 9108–9115, [https://doi.org/10.1016/s0021-9258\(17\)44637-0](https://doi.org/10.1016/s0021-9258(17)44637-0).
- [39] E. Macia, M. Ehrlich, R. Massol, E. Boucrot, C. Brunner, T. Kirchhausen, Dynasore, a cell-permeable inhibitor of dynamin, *Dev. Cell* 10 (6) (2006) 839–850, <https://doi.org/10.1016/j.devcel.2006.04.002>.
- [40] J. Saraste, G.E. Palade, M.G. Farquhar, Temperature-sensitive steps in the transport of secretory proteins through the Golgi complex in exocrine pancreatic cells, *Proc. Natl. Acad. Sci. U. S. A.* 83 (17) (1986) 6425–6429, <https://doi.org/10.1073/pnas.83.17.6425>.
- [41] W.F. Wolkers, H. Oldenhof, F. Tang, J. Han, J. Bigalk, H. Sieme, Factors affecting the membrane permeability barrier function of cells during preservation technologies, *Langmuir* 35 (23) (2019) 7520–7528, <https://doi.org/10.1021/acs.langmuir.8b02852>.
- [42] S.L. Schmid, S.D. Conner, Regulated portals of entry into the cell, *Nature* 422 (March) (2003) 37–44.
- [43] G.H. Chai, Y. Xu, S.Q. Chen, B. Cheng, F.Q. Hu, J. You, H. Yuan, Transport mechanisms of solid lipid nanoparticles across Caco-2 cell monolayers and their related Cytotoxicology, *ACS Appl. Mater. Interfaces* 8 (9) (2016) 5929–5940, <https://doi.org/10.1021/acsami.6b00821>.
- [44] M. Anko, J. Majhenc, K. Kogej, R. Sillard, Ü. Langel, G. Anderlüh, M. Zorko, Influence of stearyl and trifluoromethylquinoline modifications of the cell penetrating peptide TP10 on its interaction with a lipid membrane, *Biochim. Biophys. Acta Biomembr.* 1818 (3) (2012) 915–924, <https://doi.org/10.1016/j.bbmem.2011.12.028>.
- [45] K. Ezzat, S. El Andaloussi, E.M. Zaghoul, T. Lehto, S. Lindberg, P.M.D. Moreno, Ü. Langel, PepFect 14, a novel cell-penetrating peptide for oligonucleotide delivery in solution and as solid formulation, *Nucleic Acids Res.* 39 (12) (2011) 5284–5298, <https://doi.org/10.1093/nar/gkr072>.
- [46] S. Katayama, H. Hirose, K. Takayama, I. Nakase, S. Futaki, Acylation of octarginine: implication to the use of intracellular delivery vectors, *J. Control. Release* 149 (1) (2011) 29–35, <https://doi.org/10.1016/j.jconrel.2010.02.004>.
- [47] M. Mäe, S. EL Andaloussi, P. Lundin, N. Oskolkov, H.J. Johansson, P. Guterstam, Ü. Langel, A stearylated CPP for delivery of splice correcting oligonucleotides using a non-covalent co-incubation strategy, *J. Control. Release* 134 (3) (2009) 221–227, <https://doi.org/10.1016/j.jconrel.2008.11.025>.
- [48] S. Trier, L. Linderoth, S. Bjerregaard, T.L. Andresen, U.L. Rahbek, Acylation of glucagon-like peptide-2: interaction with lipid membranes and in vitro intestinal permeability, *PLoS One* 9 (10) (2014) 0109939, <https://doi.org/10.1371/journal.pone.0109939>.
- [49] D. Oh, A. Nasrolahi Shirazi, K. Northup, B. Sullivan, R.K. Tiwari, M. Bisoffi, K. Parang, Enhanced cellular uptake of short polyarginine peptides through fatty acylation and cyclization, *Mol. Pharm.* 11 (8) (2014) 2845–2854, <https://doi.org/10.1021/mp500203e>.
- [50] Weiqiang Cheng, Seetharama Satyanarayanan, Lee Yong Lim, Aqueous-soluble, non-reversible lipid conjugate of Salmon calcitonin: synthesis, characterization and in vivo activity, *Pharm. Res.* 24 (1) (2007) 99–110, <https://doi.org/10.1007/s11095-006-9128-9>.
- [51] Weiqiang Cheng, Lee Yong Lim, Lipeo-SCT: a novel reversible Lipidized Salmon calcitonin derivative, its biophysical properties and Hypocalcemic activity, *Eur. J. Pharm. Sci.* 37 (2) (2009) 151–159, <https://doi.org/10.1016/j.ejps.2009.02.004>.
- [52] S.F. Hedegaard, D.S. Bruhn, H. Khandelia, M. Cárdenas, H.M. Nielsen, Shuffled lipidation pattern and degree of lipidation determines the membrane interaction behavior of a linear cationic membrane-active peptide, *J. Colloid Interface Sci.* 578 (2020) 584–597, <https://doi.org/10.1016/j.jcis.2020.05.121>.
- [53] J. Wang, D. Chow, H. Heiati, W.C. Shen, Reversible lipidization for the oral delivery of salmon calcitonin, *J. Control. Release* 88 (3) (2003) 369–380, [https://doi.org/10.1016/S0168-3659\(03\)00008-7](https://doi.org/10.1016/S0168-3659(03)00008-7).
- [54] S. Adhikari, J. Moscatelli, E.M. Smith, C. Banerjee, E.M. Puchner, Single-molecule localization microscopy and tracking with red-shifted states of conventional BODIPY conjugates in living cells, *Nat. Commun.* 10 (1) (2019) 1–12, <https://doi.org/10.1038/s41467-019-11384-6>.
- [55] M.E. Berginski, S.J. Creed, S. Cochran, D.W. Roadcap, J.E. Bear, S.M. Gomez, Automated analysis of invadopodia dynamics in live cells, *PeerJ* 2014 (1) (2014), <https://doi.org/10.7717/peerj.462>.
- [56] A. Demuro, I. Parker, Imaging the activity and localization of single voltage-gated  $Ca^{2+}$  channels by Total internal reflection fluorescence microscopy, *Biophys. J.* 86 (5) (2004) 3250–3259, [https://doi.org/10.1016/S0006-3495\(04\)74373-8](https://doi.org/10.1016/S0006-3495(04)74373-8).
- [57] M. Hashizume, T. Douen, M. Murakami, A. Yamamoto, K. Takada, S. Muranishi, Improvement of large intestinal absorption of insulin by chemical modification with palmitic acid in rats, *J. Pharm. Pharmacol.* 44 (7) (2011) 555–559, <https://doi.org/10.1111/j.2042-7158.1992.tb05463.x>.
- [58] R.B. Shah, M.A. Khan, Regional permeability of salmon calcitonin in isolated rat gastrointestinal tracts: transport mechanism using Caco-2 cell monolayer, *AAPS J.* 6 (4) (2004) 2–6.

- [59] M. Cetin, Y.S. Youn, Y. Capan, K.C. Lee, Preparation and characterization of salmon calcitonin-biotin conjugates, *AAPS PharmSciTech* 9 (4) (2008) 1191–1197, <https://doi.org/10.1208/s12249-008-9165-2>.
- [60] S. Kim, H. Lee, S. Lee, S.K. Kim, Y.K. Lee, B.H. Chung, Y. Byun, Enhancing effect of chemically conjugated deoxycholic acid on permeability of calcitonin in Caco-2 cells, *Drug Dev. Res.* 64 (2) (2005) 129–135, <https://doi.org/10.1002/ddr.10423>.
- [61] K.H. Song, S.J. Chung, C.K. Shim, Enhanced intestinal absorption of salmon calcitonin (sCT) from proliposomes containing bile salts, *J. Control. Release* 106 (3) (2005) 298–308, <https://doi.org/10.1016/j.jconrel.2005.05.016>.
- [62] S. Ramanathan, S. Pooyan, S. Stein, P.D. Prasad, J. Wang, M.J. Leibowitz, P. J. Sinko, Targeting the sodium-dependent multivitamin transporter (SMVT) for improving the oral absorption properties of a retro-inverso tat nonapeptide, *Pharm. Res.* 18 (7) (2001) 950–956, <https://doi.org/10.1023/A:1010932126662>.
- [63] S. Ramanathan, B. Qiu, S. Pooyan, G. Zhang, S. Stein, M.J. Leibowitz, P.J. Sinko, Targeted PEG-based bioconjugates enhance the cellular uptake and transport of a HIV-1 TAT nonapeptide, *J. Control. Release* 77 (3) (2001) 199–212, [https://doi.org/10.1016/S0168-3659\(01\)00474-6](https://doi.org/10.1016/S0168-3659(01)00474-6).